Blob/Hole Generation in the Divertor Leg of the Large Helical Device

Hirohiko TANAKA[a)], Noriyasu OHNO, Yoshiyuki TSUJI, Shin KAJITA[1)], Suguru MASUZAKI[2)], Masahiro KOBAYASHI[2)], Tomohiro MORISAKI[2)], Akio KOMORI[2)] and the LHD Experimental Group[2)]

Graduate School of Engineering, Nagoya University, Nagoya, Aichi 464-8603, Japan
[1)]*EcoTopia Science Institute, Nagoya University, Nagoya, Aichi 464-8603, Japan*
[2)]*National Institute for Fusion Science, Toki 509-5292, Japan*

(Received 15 May 2012 / Accepted 20 September 2012)

We have analyzed ion saturation current fluctuation measured by a fast scanning Langmuir probe (FSP) in edge region of the Large Helical Device (LHD). Positive and negative spikes of the ion saturation current were observed in the private region and on the divertor leg, respectively. It was found that the boundary position between these regions corresponds to the low-field side (LFS) edge of the divertor leg where the gradient of the ion saturation current profile was the maximum. Such a positional relationship resembles that near the separatrix in the LFS in tokamaks, where blobs and holes are generated. Statistical analysis indicates similar fluctuation characteristics among different magnetic devices.

Keywords: blob, hole, cross-field transport, statistical analysis, LHD

DOI: 10.1585/pfr.7.1402152

1. Introduction

Blobby plasma transport is a well-observed phenomenon in tokamak devices. Plasma blobs and holes are generated near the separatrix [1–4] where steep density and temperature gradients exist. The blobs form field-aligned structures in the scrape-off layer (SOL) [5, 6], and they are transported to the first wall across the magnetic field. They are mostly observed in the low-field-side (LFS) SOL [7–9], and they are theoretically modeled to propagate toward the LFS direction because of the $\boldsymbol{E} \times \boldsymbol{B}$ drift with an induced electric field, $\boldsymbol{E}$, which is generated by the gradient and curvature of the magnetic field, $\boldsymbol{B}$ [10]. This cross-field transport could be responsible for more than 50% of the SOL radial particle transport [11, 12]. Therefore, it is important to clarify the mechanism of the blobby plasma transport.

To improve the modeling accuracy, comparison between experiments with various magnetic configurations is a valid procedure. In the Large Helical Device (LHD), detailed statistical analysis of ion saturation current, I_{sat}, signals has been performed using Langmuir probe arrays on divertor plates [13–15]. Positive and negative spikes of I_{sat} were observed at the LFS and inside the strike point, [13]; they were interpreted as the appearance of blobs and holes, respectively. In addition, the propagation of positive spikes toward the LFS direction was observed on the divertor plate [15]. These results suggest that blobs and holes may be generated in the upstream region near the strike point. Actually, positive spikes were clearly confirmed in the edge region by two-dimensional (2D) thermal lithium-beam data analysis [16]; however, the spatial resolution of this method was relatively low (~ 5 cm) relative to the typical radial size of the blobs in tokamaks.

A fast scanning Langmuir probe (FSP) meets the requirements for blob measurements with high spatial resolution in the upstream region. Reference [17] shows the existence of positive and negative spikes near the divertor leg; however, no detailed analysis and comparison with tokamaks was not included.

In this paper, we describe the I_{sat} fluctuation measured by the FSP, and discuss in detail characteristics near the divertor leg. To improve the interpretation, we investigate the magnetic field configuration around the FSP with the KMAG code [18]. We compare the fluctuation characteristics in the LHD with those in tokamaks.

In the following section, the experimental setup is briefly described. In Sec. 3, the analysis of the magnetic configuration around the FSP and I_{sat} fluctuation are shown in sequence. The interpretation of the results is presented in Sec. 3.3, and conclusion is given in Sec. 4.

2. Experimental Setup

The LHD is the world's largest heliotron-type device (major radius R of the vessel axis is 3.9 m) equipped with two superconducting helical coils with a toroidal period number, $m = 10$. To avoid confusion, we define names for

author's e-mail: tanaka.hirohiko@lhd.nifs.ac.jp
[a)] Present address: National Institute for Fusion Science, Toki 509-5292, Japan

the magnetic regions as specified below. Figure 1 shows vertically and horizontally elongated poloidal cross sections in the LHD. They appear alternatively every 18° in the toroidal direction. The core plasma is surrounded by the ergodic region, which has a complicated magnetic configuration with a long connection length, L_c, of the magnetic field lines [19, 20]. The private region lies between the two divertor legs. The SOL region is defined as a region except for the core and private regions in the vacuum vessel.

The SOL region is located in front of the helical coils. Therefore, for a large part of the SOL region, the LFS ($-\nabla B$) direction points to the core region with high plasma pressure, P. In contrast, the private region is the furthermost from the helical coils. Thus, the LFS direction from the divertor leg points to the private region.

In this study, we analyzed the I_{sat} fluctuation measured using the FSP [17] in an inward-shifted configuration (R_{ax} = 3.6 m, see Table 1). The FSP was installed on the top of the vessel at a toroidal angle, $\phi \sim 19.5°$. A positive sign of ϕ points to the anti-clockwise direction in the torus (referred to as "ctr-direction"), and the negative sign points to the clockwise-direction (referred to as "co-direction"). The sampling frequency was 1 MHz. The graphite probe electrode was dome-shaped with a radius of 1 mm.

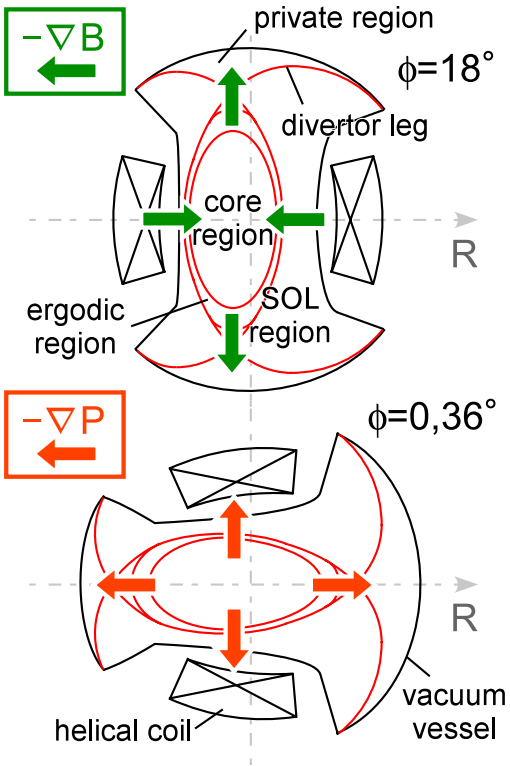

Fig. 1 Vertical and horizontal cross section of the LHD.

Table 1 List of the experimental conditions, showing the shot number, position of magnetic axis R_{ax}, toroidal magnetic field B_t, coil pitch parameter γ, and quadruple magnetic components B_q.

Shot number	R_{ax}	B_t	γ	B_q
76557	3.6 m	2.75 T	1.25	100%

3. Analysis and Discussion

First, we investigated the magnetic field configuration around the FSP. Subsequently, we analyzed the I_{sat} fluctuation measured by the FSP.

3.1 Magnetic field configuration around the FSP

Figure 2 shows a Poincaré plot of the magnetic field lines with $L_c > 20$ m at a toroidal angle $\phi_0 \approx 19.5°$ where the FSP was installed. Here, the magnetic field lines were traced from the divertor plates and terminated when they reached the wall or rotated one toroidal turn. The ergodic region with a slightly distorted rugby-ball shape is seen with its center at $R \approx 3.75$ m.

The FSP was inserted downward during a steady-state discharge. The probe head cuts across the private region and divertor leg; finally, it reaches the ergodic region. The insertion speed was $\sim$ 2 m/s, which was sufficiently slow compared with the typical radial velocity for the blob propagation reported in several tokamaks (from a few hundred to few thousand meters per second) [6, 11, 12]. Therefore, the FSP could be assumed to remain stationary relative to the blobby plasma transport.

Figure 3 (a) shows L_c profiles as a function of distance from the midplane, z. Here, the starting positions of the magnetic field line tracing were aligned on the insertion trajectory of the FSP. The magnetic field lines were traced toward the co- and ctr-directions. The co- and ctr-traced

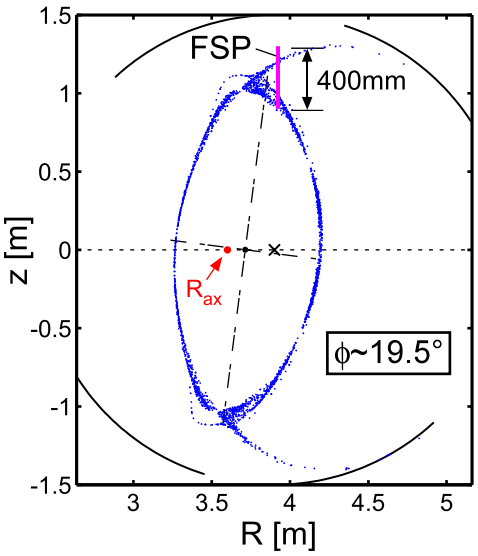

Fig. 2 Poincaré plot at $\phi_0 \approx 19.5°$ where the FSP was installed.

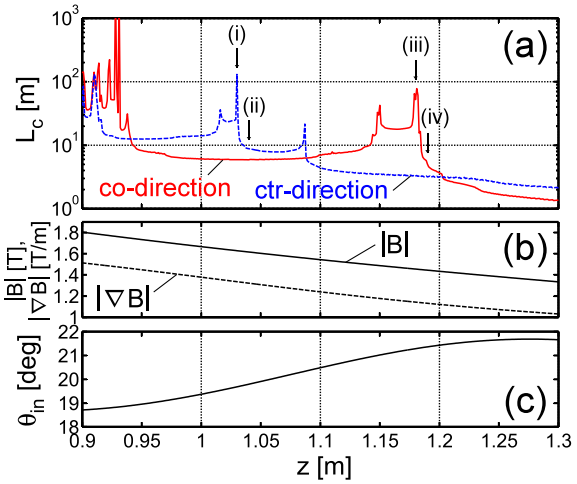

Fig. 3 (a) Profiles of the magnetic field connection lengths L_c, which are traced from the FSP insertion trajectory toward the co- (red solid line) and ctr-directions (blue dashed line). (b) Local amplitude of the magnetic field, $|\boldsymbol{B}|$ (solid line) and the gradient of B, $|\nabla B|$ (dashed line), on the insertion trajectory. (c) The angle of the insertion direction of the FSP, $\theta_{\rm in}$, which was defined by Eq. (1), along the z axis.

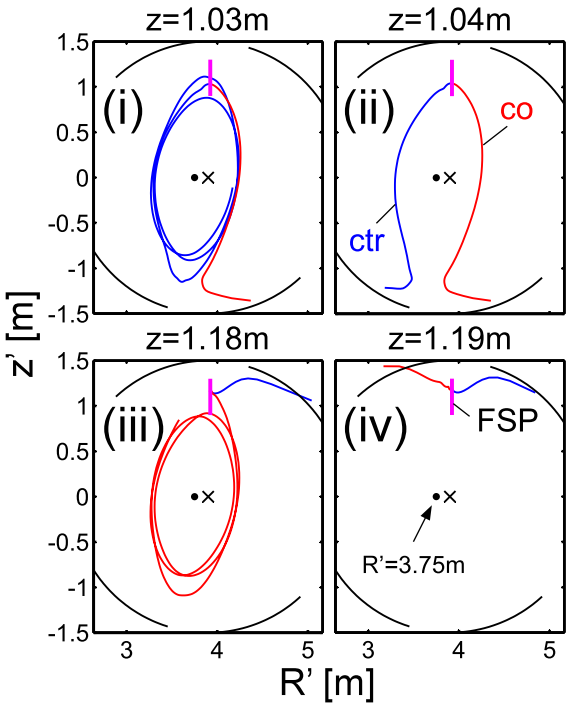

Fig. 4 Magnetic field lines mapping the same poloidal cross section with the FSP. They are traced toward the co- (red line) and crt-directions (blue line) from the FSP at z = (i) 1.03 m, (ii) 1.04 m, (iii) 1.18 m, and (iv) 1.19 m.

L_c are longer than 100 m near $z = 0.9$ m, which is in the ergodic region. The co-traced L_c is longer than $2\pi R_{\rm ax}$(∼ 23 m) at 1.15 m $< z <$ 1.18 m except for the ergodic region. On the other hand, the ctr-traced L_c over $2\pi R_{\rm ax}$ is located at 1.02 m $< z <$ 1.03 m. As described later, they are in the divertor leg and the divertor channel, respectively.

In general, blobs are long along magnetic field lines. Therefore, it is important to obtain the magnetic field geometry not only in cross section but also in successive cross sections at other toroidal angles. In the helical device, the flux tube traces a complex trajectory compared with that in tokamaks. Below, considering the simple rotation of the poloidal cross section with two helical coils, the magnetic field lines traced from the FSP were easily mapped to a single cross section at $\phi = \phi_0$. To obtain the mapped figure, we assumed that the magnetic geometry had point symmetry and a single center in all poloidal cross sections.

Figure 4 shows the magnetic field lines that are mapped on the same poloidal cross section (R', z') at ϕ_0. In this calculation, the center of all poloidal cross sections was set at $(R, z) = (3.75\,\text{m}, 0\,\text{m})$, which is near that of the ergodic region (see Fig. 2). Here, the magnetic field lines were traced from z = (i) 1.03 m, (ii) 1.04 m, (iii) 1.18 m, and (iv) 1.19 m on the insertion trajectory of the FSP. These positions are depicted in Fig. 3 (a). This tracing was terminated when each magnetic field line reached the wall or rotated one toroidal turn, as well as the magnetic field tracing in Fig. 2.

By the mapping, the positional relationship between each magnetic field line and divertor plates can be easily understood. In Fig. 4 (iii), at $z = 1.18$ m, the magnetic field line traced in the co-direction penetrates deep inside the ergodic region. On the other hand, the ctr-traced magnetic field line is immediately terminated at the divertor plate. Thus, the FSP is inside the divertor leg at $z = 1.18$ m. In Fig. 4 (i), at $z = 1.03$ m, the ctr-traced magnetic field penetrates the ergodic region, whereas the magnetic field line traced in the co-direction rotates halfway around the core region and reaches the divertor plate. This is in the divertor channel. Meanwhile, Figs. 4 (ii) and (iv) show completely different characteristics. The magnetic field lines connecting to the FSP at z = (ii) 1.04 m and (iv) 1.19 m are located in the SOL and private regions, respectively. In the latter case, the connection length between the two divertor plates is only several meters.

Figure 3 (b) shows the local magnetic field strength, $|\boldsymbol{B}|$, and the gradient of B, $|\nabla B|$, on the insertion trajectory of the FSP. The local B monotonically decreases with z, indicating that the z axis points to the LFS direction on the insertion trajectory.

To investigate the insertion angle of the FSP with respect to the theoretical direction of the blob propagation, the angle between the z axis and the gradient vector of the magnetic field, $\theta_{\rm in}$, was calculated from the following equation:

$$\theta_{\rm in} = \arccos\left(-(\nabla B)_z / |\nabla B|\right), \qquad (1)$$

where $(\nabla B)_z$ is the z-axial component of ∇B. The calcu-

lated θ_{in} profile is shown in Fig. 3 (c). The value of θ_{in} is almost constant at around 20°. If blobs propagate toward the theoretical direction, the facing surface of the probe head is slightly tilted against the blob propagation and the effective area of the probe surface is nearly constant.

3.2 Fluctuation signal measured by the FSP

Figure 5 (a) shows the I_{sat} profile measured by the FSP along the z axis. In the ergodic region near $z = 0.9$ m, I_{sat} is large. In addition, two peaks of I_{sat} are confirmed corresponding to the long L_c ($> 2\pi R_{ax}$) regions in Fig. 3 (a).

To investigate the existence of the blobs and holes, we calculated the skewness that is the third-order central moment normalized by the second-order central moment to the power of 3/2. In general, skewness is positive when blobs are detected; in contrast, skewness is negative when holes appear.

In this study, second- and third-order central moments, m_2 and m_3, respectively, were calculated using the following formulae:

$$m_2 \equiv \langle (I_{sat} - \langle I_{sat} \rangle_m)^2 \rangle_m = \langle I_{sat}^2 \rangle_m - \langle I_{sat} \rangle_m^2, \quad (2)$$

$$m_3 \equiv \langle (I_{sat} - \langle I_{sat} \rangle_m)^3 \rangle_m = \langle I_{sat}^3 \rangle_m - 3\langle I_{sat}^2 \rangle_m \langle I_{sat} \rangle_m + 2\langle I_{sat} \rangle_m^3, \quad (3)$$

where $\langle\ \rangle_m$ is the 1,000 points (1 ms) simple moving average. Then, the skewness was obtained as follows:

$$S = m_3 / m_2^{3/2}. \quad (4)$$

In this experiment, the FSP moves ~ 2 mm for 1 ms in the $(-z)$ direction.

In Fig. 5 (b), the skewness calculated by Eq. (4) is plotted as a function of z. It has a large scatter due to noise when I_{sat} is small. There are two negative peaks at $z = 1.02$ m and 1.18 m that correspond to the divertor channel and the divertor leg, respectively. On the other hand, skewness is positive over a wide range inside the private region. As the dominant component of the frequency of the I_{sat} spikes is at more than 10 kHz, which will be described later, we calculated the skewness again after applying a high-pass filter ($f > 10$ kHz) to the I_{sat} signal. Large scatter disappeared, as shown in Fig. 5 (b). Skewness with the high-pass filter also shows the above-mentioned positive and negative values.

In tokamaks, the change from negative to positive skewness is observed near the LFS separatrix, where the blobs and holes are thought to be generated [1–4]. Below, we focus on the statistics of the I_{sat} fluctuation at 1.182 m $\le z \le$ 1.194 m where the skewness changes from negative to positive along the z axis.

Figure 5 (c) shows a magnified view of I_{sat}. In addition, in this figure, the standard deviation, $\sigma = m_2^{1/2}$, and skewness are depicted. The amplitude of I_{sat} on the divertor leg at $z > 1.186$ mm rapidly decreases by approximately half within 4 mm along the z axis. The normalized I_{sat} gradient, $(dI_{sat}/dz)/I_{sat}$, is ~ 180 m^{-1} at $z = 1.188$ m where the skewness is almost zero. Referring to Fig. 3 in Ref. [2], the normalized radial gradient of I_{sat} in JET tokamak was 80–110 m^{-1} near the separatrix where the skewness was also almost zero. Therefore, the edge of the LHD divertor leg has steep normalized gradient as well as near the separatrix in tokamaks. It is also seen that σ is maximum where skewness becomes zero. At the high-field side (HFS), the skewness is negative, whereas it is positive at LFS.

The above analysis indicates that blobs and holes would be generated near the LFS edge of the divertor leg as well as near the LFS separatrix in tokamaks. In addition, the generated blobs propagate into the private region because of the gradient and curvature of magnetic field. Below, we compare the detailed statistical features of I_{sat} between the LHD and tokamaks.

The skewness does not contain temporal information. Thus, we applied wavelet analysis and expand I_{sat} to the

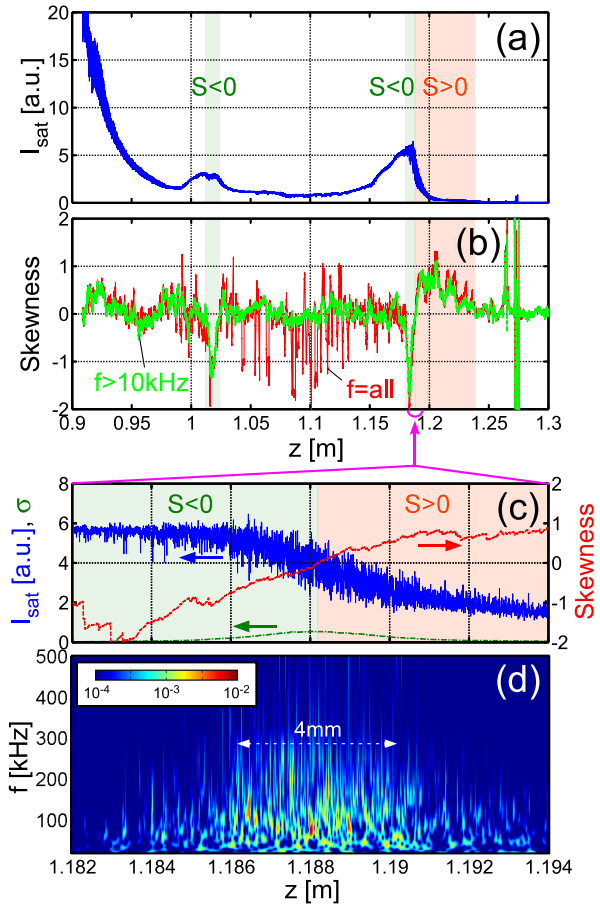

Fig. 5 (a) Profiles of I_{sat}, (b) skewness (red solid line) and skewness of the high-passed I_{sat} at $f > 10$ kHz (green dashed line) along the z axis. (c) Magnified views of I_{sat} (blue solid line), standard deviation σ (green chain line), and skewness (red dashed line). (d) Square of the absolute value of the wavelet coefficient.

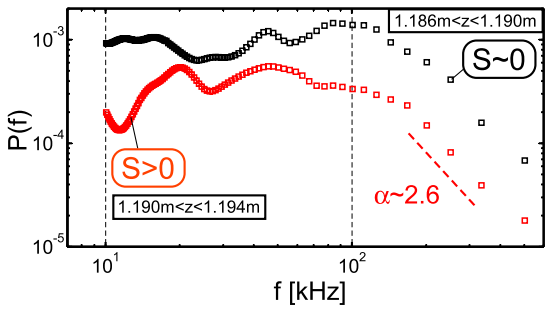

Fig. 6 Wavelet power spectra at 1.186 m $< z <$ 1.19 m (black) and 1.19 m $< z <$ 1.194 m (red).

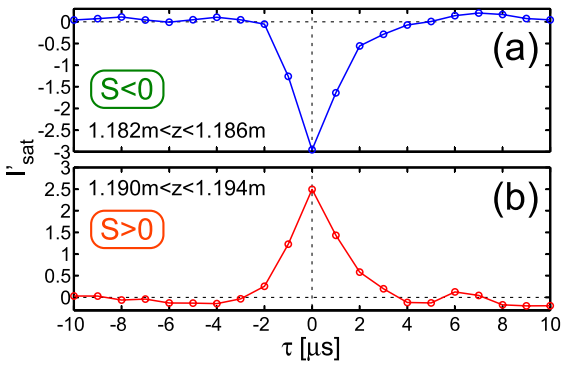

Fig. 7 Conditional averaged I'_{sat} at (a) 1.182 m $< z <$ 1.186 m and (b) 1.19 m $< z <$ 1.194 m where I'_{sat} is the moving normalized I_{sat} defined by Eq. (6); threshold values are -2 and 2, respectively.

time-frequency domain. In this study, the continuous wavelet transform [21] was performed with the complex Morlet mother wavelet,

$$\psi(t) = \pi^{1/4} \exp\left[i2\pi f_0 t - \left(t^2/2\right)\right]. \quad (5)$$

Here, the central frequency of the mother wavelet, f_0, was set at 1 kHz. Figure 5 (d) shows the square of the absolute value of the wavelet coefficient. High-frequency components strongly appear around 100 kHz at around $z = 1.188$ m that is near the position where the gradient of I_{sat} is maximum.

Figure 6 shows the wavelet power spectra at 1.186 m $< z <$ 1.19 m and 1.19 m $< z <$ 1.194 m, where the skewness is almost zero and positive, respectively. Specific differences between them cannot be found. There are no clear peaks, and they seem to have a shoulder at around 100 kHz. The shoulder consisted of a low-frequency flat region and a high-frequency diagonal region. Such a shoulder is observed when the dominant spikes have an almost constant duration time and appear nonperiodically in the fluctuation [9]. Thus, the frequency range of I_{sat} spikes is at more than 10 kHz. A power spectrum having a shoulder is commonly observed among the LFS SOLs of several tokamaks [22]. The power law ($P(f) \propto f^{-\alpha}$) scaling exponent in the high-frequency range, $\alpha \approx 2.6$, is relatively high compared with that in tokamaks ($\alpha \approx 1.6$). A large α implies that the dominant spikes are not sharply peaked. Thus, the typical density profile of the blobs in the LHD is somewhat different.

To obtain the typical shapes of the positive and negative spikes, the conditional averaging method [2, 9, 12, 22] was employed. Before applying the conditional averaging method, we used the moving normalization technique defined by the following equation:

$$I'_{sat} = \left(I_{sat} - \langle I_{sat}\rangle_m\right)/m_2^{1/2}. \quad (6)$$

Figure 7 shows the conditional averaged shapes of I'_{sat} at 1.182 m $< z <$ 1.186 m and 1.19 m $< z <$ 1.194 m, which correspond to the regions where the skewness is negative and positive, respectively. In Fig. 7 (a), large spikes of I'_{sat} with a negative peak smaller than -2 were extracted and averaged in the same time domain. Similarly, in Fig. 7 (b), large spikes of I'_{sat} with a positive peak larger than 2 were detected. With respect to time scale, the conditional I'_{sat} shapes have similar features. Thus, to a large extent, there should be a common mechanism in the determination of blob's and hole's behaviors near the generation position. In both cases, $|I'_{sat}|$ increases rapidly at $\tau < 0$, and then, $|I'_{sat}|$ gradually decreases at $\tau > 0$. This tendency is in agreement with tokamaks [2].

The time duration that the averaged I'_{sat} exceeds the offset level is $\sim 8\,\mu$s, which is much shorter than that reported in many tokamaks, such as Tore Supra [22], Alcator C-Mod [22], MAST [22], T-10 [12], JT-60U [9], and JET [2]. However, the time duration is comparable to that near the separatrix in DIII-D [11]. The time duration of the positive spike is interpreted as the typical size of blobs divided by the propagation speed. Therefore, the ratio of the size to the velocity near the divertor leg in the LHD is smaller than that in many tokamaks. Moreover, this result suggests that measurements in the LHD need high-frequency digitizers.

3.3 Discussion

In the previous section, it was found that blobs and holes would be generated in the divertor leg, which is facing the private region, as shown in Figs. 4 (iii) and (iv). In contrast, around the divertor channel at $z \sim 1.02$ m in Fig. 5 (b), only negative skewness (holes) is observed and the positive skewness is not clear. The divertor channel is next to the flux tube that passes through the SOL region, as shown in Fig. 4 (ii). Thus, it seems difficult for blobs to propagate in the SOL region compared with the private region.

This result should be discussed with respect to the magnetic configuration. On the flux tube inside the private region, the ∇B and ∇P vectors point to roughly the same direction. Thus, once a blob is ejected inside the private region, it moves to the low-density region just like a LFS SOL in tokamak devices. On the other hand, in large

parts of the SOL region, ∇B and ∇P point to opposite directions, as shown in Fig. 1. In addition, the angle between these vectors approaches zero near the X-point. Therefore, the theoretical direction of blob propagation notably varies with the location on the same flux tube that passes through the SOL region. Unlike the private region, the blob's behavior in the SOL region is complicated.

4. Conclusion

We have analyzed the magnetic field configuration and electrostatic fluctuation with high temporal and high spatial resolution in the LHD. By magnetic field tracing, the Poincaré plot and its mapping to the same poloidal cross section were presented where the FSP was installed. Statistical analysis clarified the detailed characteristics of the I_{sat} fluctuation measured by the FSP, and the results were compared with those reported in tokamaks.

Positive and negative spikes were observed in the LFS edge of the divertor leg facing the private region. The maximum gradient of the I_{sat} profile is near the boundary where the skewness is almost zero. These are similar results with those reported near the LFS separatrix in tokamaks. Thus, in the LHD, blobs would be generated in the divertor leg and propagate into the private region. Wavelet and conditional averaging analysis point to qualitative similarities with tokamaks. In the private region, blobs are not generated in the core region (closed-field region) but the divertor leg (open-field region). Therefore, the transport does not directly influence the confinement particle and energy losses.

In this study, quantitative data of parameters such as velocity and size could not be obtained. In future, we will utilize a multipin head and measure fluctuations with high temporal resolution.

Acknowledgment

This research was supported by NIFS/NINS under the project of Formation of International Network for Scientific Collaborations. This work was also performed under the auspices of the NIFS Collaboration Research program (NIFS10KLPF003), and a Grant-in-Aid for JSPS Fellows and KAKENHI (23860064).

[1] J.A. Boedo, D.L. Rudakov, R.A. Moyer, G.R. McKee, R.J. Colchin, M.J. Schaffer, P.G. Stangeby, W.P. West, S.L. Allen, T.E. Evans, R.J. Fonck, E.M. Hollmann, S. Krasheninnikov, A.W. Leonard, W. Nevins, M.A. Mahdavi, G.D. Porter, G.R. Tynan, D.G. Whyte and X. Xu, Phys. Plasmas **10**, 1670 (2003).

[2] G.S. Xu, V. Naulin, W. Fundamenski, C. Hidalgo, J.A. Alonso, C. Silva, B. Goncalves, A.H. Nielsen, J.J. Rasmussen, S.I. Krasheninnikov, B.N. Wan, M. Stamp and JET EFDA Contributors, Nucl. Fusion **49**, 092002 (2009).

[3] J. Cheng, L.W. Yan, W.Y. Hong, K.J. Zhao, T. Lan, J. Qian, A.D. Liu, H.L. Zhao, Yi. Liu, Q.W. Yang, J.Q. Dong, X.R. Duan and Y. Liu, Plasma Phys. Control. Fusion **52**, 055003 (2010).

[4] B. Nold, G.D. Conway, T. Happel, H.W. Müller, M. Ramisch, V. Rohde, U. Stroth and the ASDEX Upgrade Team, Plasma Phys. Control. Fusion **52**, 065005 (2010).

[5] R.J. Maqueda, G.A. Wurden, S. Zweben, L. Roquemore, H. Kugel, D. Johnson, S. Kaye, S. Sabbagh and R. Maingi, Rev. Sci. Instrum. **72**, 931 (2001).

[6] O. Grulke, J.L. Terry, B. Labombard and S.J. Zweben, Phys. Plasmas **13**, 012306 (2006).

[7] J.L. Terry, S.J. Zweben, K. Hallatschek, B. LaBombard, R.J. Maqueda, B. Bai, C.J. Boswell, M. Greenwald, D. Kopon, W.M. Nevins, C.S. Pitcher, B.N. Rogers, D.P. Stotler and X.Q. Xu, Phys. Plasmas **10**, 1739 (2003).

[8] G.S. Kirnev, V.P. Budaev, S.A. Grashin, L.N. Khimchenko and D.V. Sarytchev, Nucl. Fusion **45**, 459 (2005).

[9] H. Tanaka, N. Ohno, N. Asakura, Y. Tsuji, H. Kawashima, S. Takamura, Y. Uesugi and the JT-60U Team, Nucl. Fusion **49**, 065017 (2009).

[10] S.I. Krasheninnikov, Phys. Lett. A **283**, 368 (2001).

[11] J.A. Boedo, D. Rudakov, R. Moyer, S. Krasheninnikov, D. Whyte, G. McKee, G. Tynan, M. Schaffer, P. Stangeby, P. West, S. West, S. Allen, T. Evans, R. Fonck, E. Hollmann, A. Leonard, A. Mahdavi, G. Porter, M. Tillack and G. Antar, Phys. Plasmas **8**, 4826 (2001).

[12] G.S. Kirnev, V.P. Budaev, S.A. Grashin, E.V. Gerasimov and L.N. Khimchenko, Plasma Phys. Control. Fusion **46**, 621 (2004).

[13] N. Ohno, S. Masuzaki, H. Miyoshi, S. Takamura, V.P. Budaev, T. Morisaki, N. Ohyabu and A. Komori, Contrib. Plasma Phys. **46**, 692 (2006).

[14] J.M. Dewhurst, B. Hnat, N. Ohno, R.O. Dendy, S. Masuzaki, T. Morisaki and A. Komori, Plasma Phys. Control. Fusion **50**, 095013 (2008).

[15] H. Tanaka, N. Ohno, Y. Tsuji, S. Kajita, S. Masuzaki, M. Kobayashi, T. Morisaki, H. Tsuchiya, A. Komori and the LHD Experimental Group, Phys. Plasmas **17**, 102509 (2010).

[16] H. Tsuchiya, T. Morisaki, V. P. Budaev, A. Komori, H. Yamada and the LHD Experimental Group, Plasma Fusion Res. **5**, S2078 (2010).

[17] S. Masuzaki, N. Ohno, V.P. Budaev, S. Sakakibara, T. Morisaki, M. Kobayashi, N. Ohyabu, A. Komori and the LHD Experimental Group, Proceedings of ITC/ISHW2007, Toki, Japan (2007).

[18] Y. Nakamura, M. Wakatani and K. Ichiguchi, J. Plasma Fusion Res. **69**, 41 (1993).

[19] T. Morisaki, S. Sakakibara, K. Watanabe, H. Yamada, S. Masuzaki, N. Ohyabu, A. Komori, K. Yamazaki and O. Motojima, Contrib. Plasma Phys. **40**, 266 (2000).

[20] S. Masuzaki, T. Morisaki, N. Ohyabu, A. Komori, H. Suzuki, N. Noda, Y. Kubota, R. Sakamoto, K. Narihara, K. Kawahata, K. Tanaka, T. Tokuzawa, S. Morita, M. Goto, M. Osakabe, T. Watanabe, Y. Matsumoto, O. Motojima and the LHD Experimental Group, Nucl. Fusion **42**, 750 (2002).

[21] N. Ohno, V.P. Budaev, K. Furuta, H. Miyoshi and S. Takamura, Contrib. Plasma Phys. **44**, 222 (2004).

[22] G.A. Antar, G. Counsell, Y. Yu, B. Labombard and P. Devynck, Phys. Plasmas **10**, 419 (2003).